

Emergent spin-liquid-like state in the bond-disordered breathing pyrochlore

Suheon Lee

Chung-Ang University

Seunghwan Do

Chung-Ang University

W.-J. Lee

Chung-Ang University

Y.-S. Choi

Chung-Ang University

Johan Van Tol

NHMFL

Arneil Reyes

NHMFL <https://orcid.org/0000-0003-2638-5474>

Yurii Skourski

Helmholtz-Zentrum Dresden-Rossendorf

Wei-tin Chen

Center for Condensed Matter Sciences, National Taiwan University

K.-Y. Choi (✉ kchoi@cau.ac.kr)

Chung-Ang University <https://orcid.org/0000-0001-8213-5395>

Article

Keywords: breathing pyrochlore system, spin-liquid-like state, spin liquids, bond disorder

Posted Date: August 12th, 2020

DOI: <https://doi.org/10.21203/rs.3.rs-50493/v1>

License:  This work is licensed under a Creative Commons Attribution 4.0 International License.

[Read Full License](#)

Emergent spin-liquid-like state in the bond-disordered breathing pyrochlore

S. Lee¹, S.-H. Do¹, W. Lee¹, Y. S. Choi¹, J. van Tol², A. P. Reyes², Y. Skourski³, W.-T. Chen^{4,5}, and K.-Y. Choi^{1,†}

¹ *Department of Physics, Chung-Ang University, 84 Heukseok-ro, Seoul 06974, Republic of Korea*

² *National High Magnetic Field Laboratory, Florida State University, Tallahassee, Florida 32310, USA*

³ *Dresden High Magnetic Field Laboratory, Forschungszentrum Dresden-Rossendorf, 01314 Dresden, Germany*

⁴ *Center for Condensed Matter Sciences, National Taiwan University, Taipei 10617, Taiwan*

⁵ *Center of Atomic Initiative for New Materials, National Taiwan University, Taipei 10617, Taiwan*

Abstract

A breathing pyrochlore system is predicted to host a variety of quantum spin liquids. However, perturbations beyond nearest-neighbor Heisenberg interaction are an obstacle to identifying such exotic states. Here, we utilize a bond-alternating disorder to tune a magnetic ground state in the Cr-based breathing pyrochlore. By combining thermodynamic and magnetic resonance techniques, we provide experimental signatures of a spin-liquid-like state in $\text{LiGa}_{1-x}\text{In}_x\text{Cr}_4\text{O}_8$ ($x=0.2$), namely, a nearly T^2 -dependent magnetic specific heat and a persistent spin dynamics by muon spin relaxation (μSR). Moreover, ^7Li NMR, ZF- μSR , and ESR unveil the dichotomic nature of both temporal and thermal spin fluctuations: slowly fluctuating tetramer singlets at high temperatures and a fast fluctuating spin-liquid-like state at low temperatures. Our results suggest that a bond disorder in the breathing pyrochlore offers a new route to achieve an unexplored state of matter.

Introduction

Frustrated quantum magnets provide a fertile ground to discover exotic quantum and topological phenomena, ranging from quantum spin liquids to magnetic monopoles in spin ice to Majorana anyons in the Kitaev honeycomb lattice.^{1,2} A prominent instance is a pyrochlore lattice, which is a three-dimensional network of corner-sharing tetrahedra.³ The pyrochlore Heisenberg antiferromagnet is predicted to harbor a spin-liquid ground state in the absence of further neighbor interactions.⁴⁻⁶ In real materials, the macroscopic ground-state degeneracy can be lifted by a range of perturbations, including spin-lattice couplings, additional magnetic interactions, and quenched disorders.⁷⁻¹⁰ The lifting of the highly degenerate ground states gives rise to emergent phenomena such as zero-energy modes, quantum spin ice, quantum spin liquid, and moment fragmentations.¹¹⁻¹⁵

By the same token, bond alternation as a perturbation to the pyrochlore system leads to a new structural motif called a breathing pyrochlore lattice. Its spin Hamiltonian is described as $\mathcal{H} = J \sum_{i,j \in A} \mathbf{S}_i \cdot \mathbf{S}_j + J' \sum_{i,j \in B} \mathbf{S}_i \cdot \mathbf{S}_j$, where J and J' are the nearest-neighbor exchange interactions for the A and B tetrahedra of two alternating sizes, respectively.^{16,17} In the breathing pyrochlore, the breathing anisotropy $B_f = J'/J$ gauges a degree of the bond alternation. Remarkably, the breathing pyrochlore can host Weyl magnons in an antiferromagnetically ordered phase, as well as a fracton spin liquid in the presence of Dzyaloshinskii-Moriya interactions not to mention a Coulomb spin liquid.^{18,19}

On the material side, the Cr-based breathing pyrochlore LiACr_4O_8 ($A = \text{Ga}^{3+}, \text{In}^{3+}$; space group $\bar{F}43m$) is a particularly interesting example because B_f can be tuned by varying the composition of Li and A.¹⁷ $\text{LiGaCr}_4\text{O}_8$, having the breathing anisotropy $B_f = 0.6$, behaves much like a uniform pyrochlore. On the other hand, $\text{LiInCr}_4\text{O}_8$ has the small $B_f = 0.1$, in which the A tetrahedra are weakly coupled through inter-tetrahedral interaction J' . Despite the large difference in B_f , both the LiACr_4O_8 compounds show commonly two-stage symmetry breaking: a magnetostructural phase transition at $T_S=16$ (17) K with subsequent antiferromagnetic ordering at $T_M=13$ (14) K for $A=\text{In}$ (Ga).²⁰ The lasting magnetic orders suggest that the bond alternation alone is not sufficient to repress the effect of spin-lattice coupling that induces a cubic-to-tetragonal transition. In this situation, bond randomness can counteract the detrimental impact of the magnetoelastic transition. This raises the exciting prospect of tracing intrinsic spin dynamics of the breathing pyrochlore lattice to a putative spin-liquid ground state, not being interrupted by long-range magnetic order.

In this work, we investigate spin dynamics and low-energy excitations of the bond-disordered breathing pyrochlore $\text{LiGa}_{0.2}\text{In}_{0.8}\text{Cr}_4\text{O}_8$ by combining multiple magnetic resonances with thermodynamic techniques. We observe a thermal and temporal dichotomy between a coupled tetramer singlet and a spin-liquid-like state. Spin fluctuations probed on the different time scales give evidence that the emergent spin-liquid state is pertinent to a correlated pyrochlore lattice with dimensional reduction.

Results

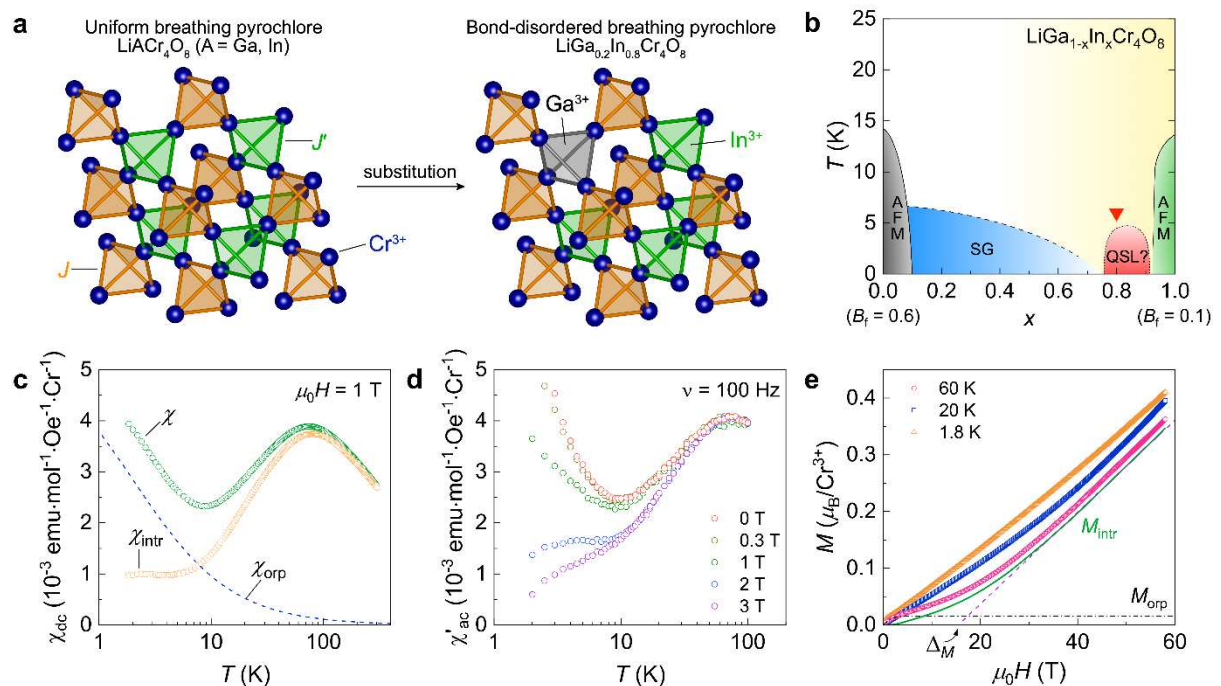


Fig. 1 | Crystal structure, phase diagram, and magnetic properties. **a** Schematic structure of the uniform breathing pyrochlore LiACr_4O_8 ($A = \text{Ga}, \text{In}$) and the bond-disordered breathing pyrochlore $\text{LiGa}_{0.2}\text{In}_{0.8}\text{Cr}_4\text{O}_8$. **b** T - x phase diagram of $\text{LiGa}_{1-x}\text{In}_x\text{Cr}_4\text{O}_8$. The inverse red triangle marks the investigated compound $\text{LiGa}_{0.2}\text{In}_{0.8}\text{Cr}_4\text{O}_8$. **c** Temperature dependence of the static magnetic susceptibility $\chi_{\text{dc}}(T)$ of $\text{LiGa}_{0.2}\text{In}_{0.8}\text{Cr}_4\text{O}_8$. $\chi_{\text{dc}}(T)$ is decomposed into the intrinsic $\chi_{\text{intr}}(T)$ and the orphan spin contribution $\chi_{\text{orp}}(T)$. **d** Real component of the ac magnetic susceptibility $\chi'_{\text{ac}}(T)$ as a function of T and B measured with a fixed frequency of $\nu = 100$ Hz. **e** High-field magnetization measured at selected temperatures. The black dashed-dotted and green dashed lines indicate the orphan spin magnetization $M_{\text{orp}}(T)$ and the bulk magnetization $M_{\text{intr}}(T)$. A linear extrapolation gives the spin gap of $\Delta_M/k_B \sim 20$ K.

Magnetic phase diagram As sketched in Fig. 1a, the A -site ordered LiACr_4O_8 ($A = \text{Ga}, \text{In}$) spinels are a nearly perfect realization of the breathing pyrochlore lattice due to the significant difference between the Li^+ and A^{3+} valence states. The Ga-for-In substitution disrupts a uniform arrangement of the two alternating tetrahedra and leads to the rich magnetic phase

diagram of $\text{LiGa}_{1-x}\text{In}_x\text{Cr}_4\text{O}_8$, as shown in Fig. 1b.²¹ The magnetic ordering vanishes for $x>0.1$ or $x<0.95$. A spin-glass phase occupies a wide range of $x=0.1 - 0.625$. For the Ga-rich compound $\text{LiGa}_{0.95}\text{In}_{0.05}\text{Cr}_4\text{O}_8$, the ^7Li NMR and neutron experiments revealed the spin nematic transition at $T_f = 11$ K, driven by the small bond disorder.²² In the In-rich range of $x=0.7 - 0.95$, $\text{LiGa}_{1-x}\text{In}_x\text{Cr}_4\text{O}_8$ exhibits a spin-gap behavior with the lack of magnetic ordering and spin freezing down to 2 K.^{21,23} However, little is known about an exact ground state. Here, we have chosen the $x=0.8$ compound (marked by the inverse triangle in Fig. 1b) to address this issue.

Magnetic susceptibilities and magnetization Figure 1c presents the T dependence of dc magnetic susceptibility $\chi_{\text{dc}}(T)$ of $\text{LiGa}_{0.2}\text{In}_{0.8}\text{Cr}_4\text{O}_8$. On cooling, $\chi_{\text{dc}}(T)$ shows a broad hump at around 70 K, and a subsequent upturn below 10 K. Above 100 K, $\chi_{\text{dc}}(T)$ follows the Curie-Weiss law with the Curie-Weiss temperature $\Theta_{\text{CW}}=-386(1)$ K and the effective magnetic moment $\mu_{\text{eff}}=3.873(4) \mu_{\text{B}}$ (see Supplementary Note 1 and Supplementary Fig. 1) that are consistent with the values in the previous report.²¹ The low- T upturn of $\chi_{\text{dc}}(T)$ is reminiscent of orphan spins. We attempt to single out the intrinsic $\chi_{\text{intr}}(T)$ by fitting the $T<5$ K data to $\chi_{\text{dc}}(T) = \chi_{\text{intr}}(T) + \chi_{\text{orp}}(T)$, where $\chi_{\text{orp}}(T)=C_{\text{orp}}/(T+ \Theta_{\text{orp}})$. We obtain $\Theta_{\text{orp}}= -2.0(2)$ K, confirming the contribution of weakly interacting orphan spins. The orphan spin concentration is estimated to be 0.6 % of the Cr^{3+} spins, smaller than the value obtained from the high-field magnetization data (see below). After the subtraction of $\chi_{\text{orp}}(T)$ from $\chi_{\text{dc}}(T)$, we can identify a nearly constant $\chi_{\text{intr}}(T<5 \text{ K})$, indicative of the presence of abundant low-energy in-gap states.

Exhibited in Fig. 1d is the real component of the ac magnetic susceptibility $\chi'_{\text{ac}}(T, B)$ as a function of T and B at a fixed frequency $\nu=100$ Hz. The low- T upturn of $\chi'_{\text{ac}}(T, B)$ is systematically suppressed with increasing B . Remarkably, $\chi'_{\text{ac}}(T, B=2 \text{ T})$ becomes nearly T independent below $T^*=10$ K. This is attributed to the Zeeman splitting of the orphan $s=3/2$ moments that weakly interact with an energy scale of $|\Theta_{\text{orp}}| \approx 2$ K. In addition, $\chi'_{\text{ac}}(T)$ shows no apparent frequency dependence, ruling out the formation of spin freezing or spin glass state (see Supplementary Note 2 and Supplementary Fig. 2).

We next turn to the high-field magnetization $M(T, B)$ measured up to 58 T at selected temperatures (see Fig. 1e). With increasing field, $M(T=1.8 \text{ K}, B)$ shows an upward convex behavior at low fields and then switches to a concave curvature at high fields. The low- B convex $M(H)$ is associated with the orphan spin contribution $M_{\text{orp}}(H)$. To separate $M_{\text{orp}}(H)$ from $M(H)$, we fit the $T=1.8$ K data to a Brillouin function B_J . The number of the orphan spins is evaluated to be 1.5 % of the Cr^{3+} spins. By subtracting $M_{\text{orp}}(H)$ from $M(H)$, we can obtain the intrinsic magnetization $M_{\text{intr}}(H)$, as illustrated by the green line in Fig. 1e. $M_{\text{intr}}(H)$ increases slowly at low fields and then exhibits a steep, linear increase above 30 T. The linear

extrapolation of the high-field $M_{\text{intr}}(H)$ yields the spin gap $\Delta_M/k_B \sim 20$ K. The finite slope of $M_{\text{intr}}(H)$ at low fields is ascribed to the in-gap state, consistent with the $\chi_{\text{dc}}(T)$ and $\chi'_{\text{ac}}(T, B)$ data. At $T=60$ K ($\gg \Delta_M/k_B$), $M(H)$ shows a quasilinear increase, characteristic of antiferromagnetically coupled spins.

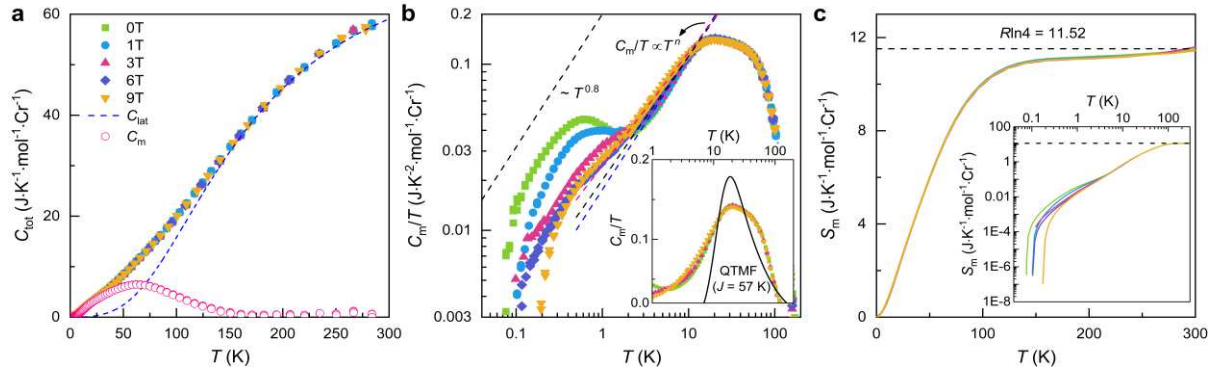


Fig. 2 | Heat capacity of the breathing pyrochlore LiGa_{0.2}In_{0.8}Cr₄O₈. **a** Temperature dependence of the total heat capacity C_{tot} in various magnetic fields $B=0, 1, 3, 6,$ and 9 T. The blue dashed curve denotes the evaluated lattice contributions using the Debye model. The open pink circles represent the magnetic heat capacity C_m . **b** Temperature and field dependences of the magnetic heat capacity divided by temperature C_m/T after subtracting the lattice and nuclear Schottky contributions on a double log scale. The dashed lines are fits to the power-law behavior $C_m/T \sim T^n$ with $n = 0.68 - 0.82$. The inset shows a comparison between the C_m/T data and the theoretical curve for a $s=3/2$ tetrahedron model. **c** Temperature dependence of the magnetic entropy S_m under various magnetic fields. The dashed black line corresponds to the theoretical value $R \ln 4 = 11.52$. The inset is a log-log plot of S_m vs. temperature.

Heat capacity To elucidate the nature of low-energy magnetic excitations, we performed heat capacity measurements down to 100 mK in various magnetic fields.

In Fig. 2, we plot the heat capacity of LiGa_{0.2}In_{0.8}Cr₄O₈ as a function of temperature. The total specific heat comprises the sum of lattice, magnetic, and nuclear contributions, $C_{\text{tot}} = C_{\text{lat}} + C_m + C_{\text{NS}}$. Here, C_{lat} represents the lattice heat capacity, C_m is the magnetic heat capacity, and C_{NS} is the nuclear Schottky contribution. To isolate the magnetic contribution C_m from C_{tot} , we estimate the lattice heat capacity C_{lat} using the Debye model and the nuclear Schottky contribution C_{NS} using $C_{\text{NS}}/T \sim T^3$ at low temperatures (see Supplementary Fig. 3a). The Debye model well reproduces the high- T C_{tot} with the Debye temperature $\Theta_D=669$ K, as shown in Fig. 2a. After subtracting the calculated C_{lat} and C_{NS} from C_{tot} , we obtain the magnetic heat capacity C_m . As evident from Fig. 2a, $C_m(T)$ shows a broad maximum around 70 K, at which both $\chi_{\text{dc}}(T)$ and $\chi'_{\text{ac}}(T, B)$ indicate the onset of short-range ordering.

From a log-log plot of C_m/T vs. T in Fig. 2b, we observe a hump at around $T = 0.6$ K in addition to the high- T broad hump. The lack of a sharp peak excludes long-range magnetic ordering. On the application of an external magnetic field, the $T = 0.6$ K hump shifts to a higher temperature and is quickly suppressed at $\mu_0 H > 3$ T. The B -dependence of the low- T hump is attributed to the weakly coupled orphan spins, which become frozen in the small field. In addition, $C_m(T)/T$ displays a moderate B dependence in the T range of $T=0.1 - 10$ K. Overall, the $C_m(T)/T$ data are described by the power-law dependence $C_m/T \sim T^n$. The exponent is determined to be $n = 0.68 - 0.82$ in the T range of $T = 2 - 10$ K and $n = 0.67 - 0.86$ below 1 K. The observed power-law behavior $C_m \sim T^{1.68 - 1.82}$ is close to the quadratic T dependence. We recall that in kagome antiferromagnets, the T^2 dependence of C_m is taken as evidence of gapless spinon excitations.^{24,25} On the other hand, the coupling between spin and orbital degrees of freedom is evoked in the pyrochlore lattice.^{26,27} Obviously, the orbital degrees of freedom are not relevant to the Cr-based breathing pyrochlore. A comparison between the C_m/T data and the calculated curve of a $s=3/2$ isolated tetrahedron unveils a large discrepancy for temperatures below 10 K (see the inset of Fig. 2b). Thus, we conclude that the observed quadratic dependence of C_m is associated with emergent low-energy excitations of the bond-disordered breathing pyrochlore. We note that the C_m/T data show a steep decrease and deviation from the power-law behavior below 0.1 K. To diagnose the presence of a spin gap, we try to fit the low- T C_m data to $C_m \sim \exp[-\Delta_{\text{low}}/k_B T]$. The extracted $\Delta_{\text{low}}/k_B \sim 0.29(1)$ K turns out to be tiny (see Supplementary Note 3 and Supplementary Fig. 3b).

Figure 2c presents the magnetic entropy $S_m(T, B)$, which was calculated by integrating C_m/T . $S_m(T, B)$ exhibits the saturation to $R \ln 4 \sim 11.52$ at 300 K, consistent with an $s=3/2$ spin system. $S_m(T, B)$ is gradually released with decreasing temperature below 100 K due to the development of short-range magnetic correlations. Only a tiny fraction of $S_m(T, B)$ remains at 0.1 K, which is less than 0.01 %. The nearly-zero residual entropy excludes any kind of magnetic transitions at low temperatures. Taken together, $\text{LiGa}_{0.2}\text{In}_{0.8}\text{Cr}_4\text{O}_8$ features a spin-liquid-like ground state with nearly gapless excitations, which evolves from the high- T coupled tetramer singlet state.

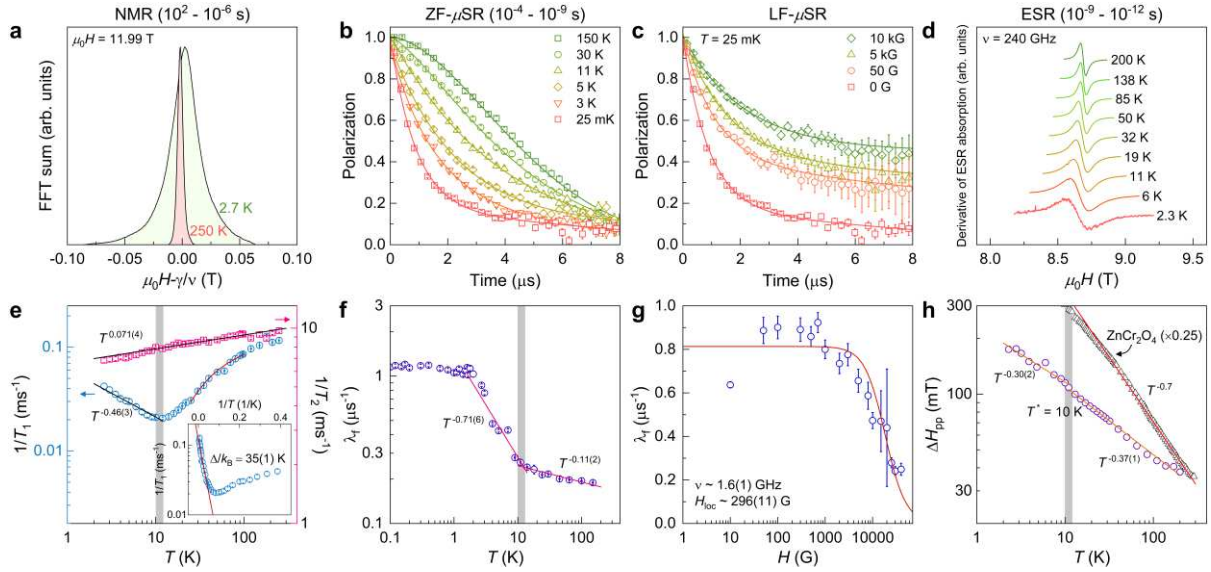


Fig. 3 | Thermal and temporal evolution of spin fluctuations of $\text{LiGa}_{0.2}\text{In}_{0.8}\text{Cr}_4\text{O}_8$ measured by ^7Li NMR, ZF- μSR , and ESR. **a** ^7Li NMR spectra obtained by integrating spin-echo intensity at $T = 2.7$ and 250 K. **b** ZF- μSR spectra at selected temperatures. **c** Longitudinal field dependence of the μSR spectra measured at $T = 25$ mK. The solid lines denote the fit to the data using the sum of two simple exponential functions. **d** Derivative of the ESR absorption spectra measured at various temperatures. Spectra are vertically shifted for clarity. **e** Temperature dependence of ^7Li spin-lattice relaxation rate $1/T_1$ and spin-spin relaxation rate $1/T_2$. The red solid line denotes the Arrhenius equation, yielding the spin gap of $\Delta/k_B = 35(1)$ K. The solid black line represents a power-law behavior of $1/T_1$ and $1/T_2$. **f** Muon spin relaxation rate as a function of temperature $\lambda_f(T)$. The solid magenta line represents the power-law fit to the data. **g** Muon spin relaxation as a function of longitudinal field $\lambda_{\text{LF}}(H)$. The red solid line represents the fit to the Redfield formula. **h** Temperature dependence of the peak-to-peak ESR linewidth $\Delta H_{\text{pp}}(T)$. The solid orange lines indicate a power-law behavior of $\Delta H_{\text{pp}}(T)$ in two different temperature regions. The shaded region indicates the change of magnetic correlations at around $T^* = 10$ K.

Nuclear magnetic resonance We now examine temporal and thermal spin fluctuations by combining multiple magnetic resonance techniques that probe spin correlations on different time scales.

The ^7Li NMR spectra and the spin-lattice (spin-spin) relaxation rate $1/T_1$ ($1/T_2$) are plotted as a function of temperature in Fig. 3a and 3e. At high temperatures, the NMR spectrum exhibits a single sharp line with no quadrupolar splitting, similarly observed in $\text{LiInCr}_4\text{O}_8$.^{20,28} As the temperature is lowered, the NMR spectra show a continuous broadening and a shift to higher magnetic fields, emulating the development of magnetic correlations and internal fields down to $T = 2.7$ K. We observe neither a structured broadening of the NMR spectrum nor a sharp peak in $1/T_1$, further confirming the absence of long-range magnetic ordering and structural phase transition.

On cooling, $1/T_1$ displays an exponential-like decrease down to 10 K, and then a subsequent upturn to a power-law growth. The activation behavior of $1/T_1$ in the T range of 25 – 100 K is well fitted with the Arrhenius equation $1/T_1 \sim \exp(-\Delta/k_B T)$ (see the semi-log plot of $1/T_1$ vs. $1/T$ in the inset of Fig. 3e). We obtain the spin gap $\Delta/k_B = 35(1)$ K, somewhat larger than $\Delta_M/k_B \sim 20$ K extracted from $M_{\text{intr}}(H)$. Generally, the spin gap Δ/k_B obtained from $1/T_1$ is larger than the true spin gap $\Delta_{\text{min}}(q)$ occurring at a specific point q .^{29–31} This is because $1/T_1$ maps out the q -average of the dynamical spin susceptibility, $1/T_1 \sim T \sum_q A^2(q) \chi''(q, \omega_0)$. Here, $A(q)$ is the form factor of hyperfine interactions, and ω_0 is the nuclear Larmor frequency.

The salient feature is that $1/T_1$ follows a power law $1/T_1 \sim T^{-n}$ with the exponent of $n = -0.46(3)$ below $T^* = 10$ K, indicative of the development of highly correlated states. The drastically distinct behavior of $1/T_1$ through $T^* = 10$ K suggests the switching of a dominant relaxation mechanism: a high- T activated vs. a low- T critical slowing-down. The spin-spin relaxation rate $1/T_2$ shows a weak power-law decrease $1/T_2 \sim T^{0.071(4)}$ as $T \rightarrow 0$. A nearly T -independent $1/T_2$ means that spin dynamics is in the fast fluctuating exchange-narrowed limit.

Muon spin relaxation (μSR) To discriminate between static and dynamic magnetism, we performed μSR experiments for $\text{LiGa}_{0.2}\text{In}_{0.8}\text{Cr}_4\text{O}_8$. In Fig. 3b, we present ZF- μSR spectra of $\text{LiGa}_{0.2}\text{In}_{0.8}\text{Cr}_4\text{O}_8$ at selected temperatures. At high temperatures, the ZF- μSR spectra show a Gaussian-like shape and gradually change to an exponential-like form. With decreasing temperature, the muon spin polarization rapidly relaxes in the initial time interval ($t = 0 - 2 \mu\text{s}$). We observe neither oscillating muon signal down to $T = 25$ mK nor a recovery to 1/3 of the initial polarization, evidencing the formation of a dynamically fluctuating state.³²

For quantitative analysis, we fitted the ZF- μSR spectra to the sum of a stretched exponential function and an exponential function, $P_z(t) = a_{\text{fast}} \exp[-(\lambda_f t)^\beta] + a_{\text{slow}} \exp[-\lambda_s t]$. Here, a_{fast} (a_{slow}) is the fraction of the fast (slow) relaxation component, and λ_f (λ_s) is the muon spin relaxation rate for the fast (slow) relaxing component. We summarize the obtained parameters in Fig. 3f and Supplementary Information (see Supplementary Fig. 4). As the temperature decreases, the slow relaxation component suddenly appears below $T^* = 10$ K, at which the ^7Li $1/T_1$ shows an upturn to the power law. Furthermore, the slow muon spin relaxation rate $\lambda_s(T)$ shows a T -independent behavior ($\lambda_s \sim 0.042 \mu\text{s}^{-1}$) below 1 K.

Figure 3f is a log-log plot of the fast relaxation rate vs. T . As the temperature is lowered, $\lambda_f(T)$ exhibits a weakly increasing T -dependence down to 10 K, and then a power-law increase with the exponent of $n = -0.71(6)$. We note that the steep increment of $\lambda_f(T)$ concurs with the leveling-off of $\chi_{\text{int}}(T)$ in Fig. 1c and the upturn of $1/T_1$ in Fig. 3e. Upon further cooling toward $T = 25$ mK, $\lambda_f(T)$ flattens out below 2 K, entering a persistent-spin-dynamical regime. Such a leveling-off of the muon spin relaxation rate is often observed in an assortment of quantum spin liquid candidates.^{33–35} With decreasing temperature, the stretched exponent β gradually decreases from $\beta = 2$ (a Gaussian-like decay) to $\beta = 1$ (an exponential decay) below $T^* = 10$ K (see

Supplementary Fig. 4b). The low- T exponential relaxation suggests the persisting spin fluctuations to $T = 25$ mK without forming frozen moments.

Shown in Fig. 3c and 3g are the LF- μ SR spectra and the LF dependence of $\lambda_f(H_{LF})$ measured at $T = 25$ mK. Remarkably, the LF- μ SR spectra exhibit substantial relaxation even at $H_{LF} = 1$ T, lending further support to the dynamic ground state. In the Redfield model $\lambda_{LF}(H) = 2\gamma_\mu^2 \langle H_{loc}^2 \rangle \nu / (\nu^2 + \gamma_\mu^2 H^2)$, the LF dependence of $\lambda_f(H_{LF})$ is related to the fluctuation frequency ν , and the fluctuating time-averaged local field $\langle H_{loc}^2 \rangle$.³⁶ Here, γ_μ is the muon gyromagnetic ratio. Fitting to the $\lambda_f(H_{LF})$ data yields $\nu = 1.6(1)$ GHz and $H_{loc} = 296(11)$ G (see Fig. 3g). We note that the fluctuation frequency is faster than the value reported thus far for spin-liquid materials while the magnitude of the local field is rather large, possibly due to a large spin number $s=3/2$.^{33,35} Taken the μ SR data together, we conclude that the emergent correlated spin state below $T^* = 10$ K has a dynamic nature of a GHz fluctuation frequency.

Electron spin resonance To take a close look at spin fluctuations on the GHz time scale, we turn to high-frequency ESR. As shown in Fig. 3d, with decreasing temperature, the ESR spectra broaden continuously down to 2.3 K and shift to a lower field. We observe no impurity signals. All of the ESR spectra are fitted with a single Lorentzian profile, suggesting that they originate solely from the correlated Cr spins. The extracted parameters are plotted as a function of temperature in Fig. 3h and Supplementary Fig. 5. The peak-to-peak linewidth ΔH_{pp} is associated with the development of spin-spin correlations, while the resonance field H_{res} reflects the build-up of internal magnetic fields.

As the temperature is lowered, $\Delta H_{pp}(T)$ exhibits a critical increase, which is described by a power-law $\Delta H_{pp}(T) \sim T^{-n}$. We can identify a small change of the exponent from $n = -0.37(1)$ to $0.30(2)$ through $T^* = 10$ K. This weak anomaly in the exponent is in sharp contrast to the drastically changing character of the magnetic correlations on the MHz time scale.

A critical line broadening in the paramagnetic state is due to the development of local spin correlations below the Curie-Weiss temperature Θ_{CW} and is generic to frustrated magnets subject to critical spin fluctuations. We note that the observed critical exponent of $n = 0.30 - 0.37$ is much smaller than $n = 0.6 - 0.7$ for the uniform pyrochlore $M\text{Cr}_2\text{O}_4$ (for $M = \text{Zn}, \text{Mg}, \text{Cd}$)³⁷, as shown in Fig. 3h. Compared to the uniform pyrochlore, the reduced exponent in $\text{LiGa}_{0.2}\text{In}_{0.8}\text{Cr}_4\text{O}_8$ is interpreted in terms of the dimensional reduction as discussed below. As such, the emergent low- T state bears a resemblance to the ground state inherent to a pyrochlore lattice.

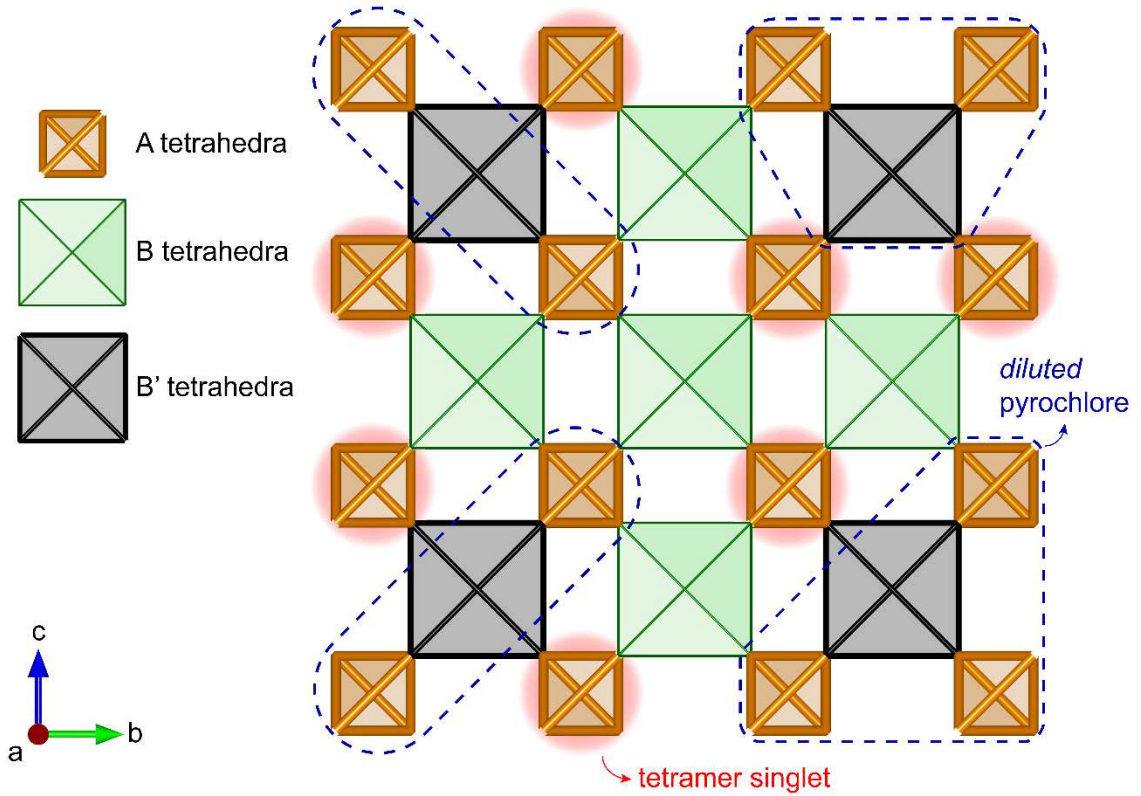


Fig. 4| Schematics of the emergent magnetic subsystems in a bond-disordered breathing pyrochlore. Each square represents the tetrahedra formed by the Cr spins. The Cr spins are omitted for clarity. The orange and green squares are the alternating A and B tetrahedra for $\text{LiInCr}_4\text{O}_8$. The grey square denotes the B' tetrahedra introduced by the Ga-for-In substitution. Due to an energy hierarchy of the tetrahedral ($E_A \sim E_{B'} > E_B$), the breathing pyrochlore is effectively decomposed into two subsystems: (i) coupled tetramer singlets (red shaded circle) and (ii) diluted pyrochlore lattices (blue dashed region).

Discussion

With the aid of various thermodynamic and magnetic resonance techniques (0 Hz – 1 THz), we are able to disclose the temporal and thermal structures of magnetic correlations in the bond-disordered breathing pyrochlore $\text{LiGa}_{0.2}\text{In}_{0.8}\text{Cr}_4\text{O}_8$.

We identify the characteristic temperature $T^* = 10$ K, below which a highly correlated spin state emerges from high- T tetramer singlet fluctuations. The emergent low-energy state features nearly T -squared C_m as well as critical spin fluctuations over a wide time scale of $10^{-12} - 10^{-4}$ sec, as evident from a power-law $1/T_1 \sim T^{-0.46(3)}$, $\lambda_f(T) \sim T^{-0.71(6)}$, and $\Delta H_{pp}(T) \sim T^{-0.30}$. We recall that the energy scale of $T^* = 10$ K is smaller than the spin gap of $\Delta/k_B = 20 - 35$ K, deduced from $M(H)$ and $1/T_1$. Yet, it is bigger than a few kelvins of weakly correlated orphan spins. The latter contribution is quenched by applying the external field of $\mu_0 H > 3$ T. As such, the low- T correlated state does not stem from extrinsic defect spins. Rather, it pertains to the in-gap magnetic state created by the bond randomness in a breathing pyrochlore. Here, we stress that

there is no hint for random singlets whose fingerprints are scalings of thermodynamic quantities, namely, $\chi(T) \sim T^{1-\alpha}$, $M(H) \sim T^\alpha$, and $C_m(T) \sim T^\alpha$ with $0 < \alpha < 1$.³⁸ Therefore, the low- T correlated state is distinct from a bond-disorder induced random singlet.

We next turn to the temporal spin dynamics. The thermodynamic data reveal the spin gap decorated with the in-gap state. On the slow time scale ($1 - 10^4$ Hz), the NMR data demonstrate a dichotomic spin dynamics, namely, high- T singlet correlations and low- T critical correlations. On the fast time scale ($10^4 - 10^{12}$ Hz), the μ SR and ESR data give no signature of the tetramer singlet correlations. Instead, highly correlated spins prevail over the whole measured temperature range and show a spin-liquid behavior. This behavior means that the singlet fluctuations average out beyond the time scale of the NMR technique at low temperatures. Another perspective is that $\text{LiGa}_{0.2}\text{In}_{0.8}\text{Cr}_4\text{O}_8$ comprises two spin subsystems whose temporal magnetic correlations differ from each other. As the tetramer singlet forms an entangled state of four spins, its spin fluctuations are slower than the spin fluctuations of the rest subsystem that are governed by two-spin correlations. In the GHz time window, the high- T critical spin dynamics persists to the low- T state. More specifically, the power-law dependence of $\Delta H_{\text{pp}}(T)$, which is an ESR signature of the pyrochlore-like spin dynamics, is observed down to $T=2.3$ K. This gives indirect evidence that the low- T in-gap state is linked to a pyrochlore-like subsystem.

Lastly, we discuss the origin of the dichotomic magnetic correlations emerging from the bond-alternating disorder in $\text{LiGa}_{0.2}\text{In}_{0.8}\text{Cr}_4\text{O}_8$. As sketched in Fig. 4, the Ga-for-In substitution introduces the B' tetrahedra randomly to the alternating A and B tetrahedra. Consequently, the perturbed system entails two different networks consisting of (i) the alternating A and B tetrahedra with $B_f=0.1$ and (ii) the alternating A and B' tetrahedra with $B_f=0.6$. Neglecting a small fraction of the alternating B and B' tetrahedra with $B_f=0.17$, the large difference in B_f brings about two subsystems: (i) coupled tetramer singlets and (ii) *diluted* pyrochlore lattices. The coupled tetramer singlets are responsible for the high- T and slow spin fluctuations. The diluted pyrochlore subsystem weakly bonded to the tetramer singlets contributes to the emergence of the low- T spin-liquid-like state. $\text{LiInCr}_4\text{O}_8$ is in the vicinity of a critical point and is proximate to a Coulomb phase.^{28,39} However, the magnetoelastic coupling does not allow for exploring this exotic phase. Nonetheless, the bond disorder offers an efficient way to overcome restrictions imposed by the magnetostructural transition. As a by-product of quenching symmetry breaking, we obtain a *finite-size* breathing pyrochlore lattice that dictates a low-energy and fast spin behavior. As such, the low- T state of $\text{LiGa}_{0.2}\text{In}_{0.8}\text{Cr}_4\text{O}_8$ may realize a diluted Coulomb spin liquid, deserving further theoretical and experimental investigations.

To conclude, we have investigated the temporal and thermal spin dynamics of a bond-disordered breathing pyrochlore compound. We find that a dichotomy of magnetic correlations

is linked to two emergent subsystems. The observed low- T spin-liquid-like state bears pertinent spin fluctuations to a diluted breathing pyrochlore lattice, which opens up a venue for a fundamentally new state.

Methods

Sample synthesis Polycrystalline samples of $\text{LiGa}_{0.2}\text{In}_{0.8}\text{Cr}_4\text{O}_8$ were synthesized by a solid-state reaction method. Stoichiometric amounts of Li_2CO_3 , Cr_2O_3 , Ga_2O_3 , and In_2O_3 were mixed in 1:4:0.2:0.8 molar ratio and thoroughly ground in a mortar. The mixture was pelletized and sintered at 800 °C in the air for 12 h. The substance was ground, pressured into pellets, and finally sintered at 1000 °C for 24 h and 1100 °C for 72 h. We checked the quality of the samples by X-ray diffraction measurements.

Magnetic properties characterization dc and ac magnetic susceptibilities were measured using a superconducting quantum interference device magnetometer and vibrating sample magnetometer (Quantum Design MPMS and VSM). High-field magnetization experiments were performed at the Dresden High Magnetic Field Laboratory using a pulsed-field magnet (20 ms duration). The magnetic moment was detected by a standard inductive method with a pick-up coil system in the field range of $\mu_0 H = 0 - 60$ T.

Heat capacity Heat capacity measurements were carried out in the temperature and field range of $T=0.03 - 300$ K and $B=0 - 9$ T using a commercial set-up of Quantum Design PPMS with a thermal relaxation method. The raw heat capacity data C_{tot}/T follow a T^{-3} power-law behavior at extremely low temperatures, corresponding to a nuclear Schottky contribution (see Supplementary Fig. 3a). After subtracting the nuclear Schottky contribution $C_{\text{NS}}/T = AT^{-3}$ from C_{tot}/T , we present the magnetic and lattice contributions to the specific heat in the main text.

Nuclear magnetic resonance ^7Li ($I = 3/2$, $\gamma_{\text{N}} = 16.5471$ MHz/T) NMR measurements were conducted at National High Magnetic Field Laboratory (Tallahassee, USA) by using a locally developed NMR spectrometer equipped with a high-homogeneity 17 T sweepable magnet. ^7Li NMR spectra were recorded by a fast Fourier transform of spin-echo signals while sweeping the field at a fixed frequency $\nu = 198.317$ MHz. The nuclear spin-lattice (spin-spin) relaxation time T_1 (T_2) was measured by a modified inversion recovery (Hahn pulse) method with $\pi/2 = 1$ μs in the temperature range of $T = 2.6 - 250$ K.

Muon spin relaxation (μ SR) μ SR measurements were carried out on the DR spectrometer ($^3\text{He}/^4\text{He}$ dilution refrigerator, $25 \text{ mK} \leq T \leq 10 \text{ K}$) at M15 beamline and the LAMPF spectrometer (^4He cryostat, $2 < T < 300 \text{ K}$) at M20 beamline in TRIUMF (Vancouver, Canada). The polycrystalline samples of $\text{LiGa}_{0.2}\text{In}_{0.8}\text{Cr}_4\text{O}_8$ were wrapped with a silver foil and then attached to the sample holder. After the mounted samples were inserted into the cryostat, μ SR spectra were measured in zero-field, longitudinal field (parallel to muon spin direction), and transverse field (perpendicular to muon spin direction).

Electron spin resonance (ESR) High-frequency ESR experiments were performed at National High Magnetic Field Laboratory (Tallahassee, USA). The ESR spectra were recorded using a quasi-optical heterodyne spectrometer in the temperature range of $T = 2 - 290 \text{ K}$,⁴⁰ enabling the detection of a magnetic field derivative of a microwave absorption signal. An external magnetic field was swept with a 12.5 T sweepable superconducting magnet at the fixed frequency $\nu = 240 \text{ GHz}$.

Acknowledgments

We would like to thank B. Hitti for the technical support with μ SR experiments. We appreciate G. Stenning for assistance on the heat capacity measurements in the Materials Characterization Laboratory at the ISIS Neutron and Muon Source. We thank F. C. Chou for the ac susceptibility measurements and fruitful discussion. The work was supported by the National Research Foundation (NRF) of Korea (Grant no. 2020R1A2C3012367). A portion of this work was performed at the National High Magnetic Field Laboratory, which is supported by the National Science Foundation Cooperative Agreement No. DMR-1157490 and No. DMR-1644779 and the State of Florida. We acknowledge the support of the HLD at HZDR, a member of the European Magnetic Field Laboratory (EMFL).

Author contributions

K.-Y.C. designed and conceived the study. S.L., S.-H.D, and K.-Y.C. planned the experiments. S.-H.D. and Y.S.C. synthesized the sample and characterized structural and magnetic properties. W.L. and A.P.R. conducted NMR experiments. S.L. and W.L. performed μ SR experiments, and S.L. analyzed the data. S.L. and J.V.T. carried out the high-field ESR measurements. S.L. carried out the heat capacity measurements. S.L. and K.-Y.C. wrote the manuscript with contributions from all authors.

Additional information

References

1. Savary, L. & Balents, L. Quantum spin liquids: a review. *Reports on Progress in Physics* **80**, 016502 (2016).
2. Kitaev, A. Anyons in an exactly solved model and beyond. *Annals of Physics* **321**, 2–111 (2006).
3. Lee, S.-H. *et al.* Frustrated Magnetism and Cooperative Phase Transitions in Spinels. *Journal of the Physical Society of Japan* **79**, 011004 (2010).
4. Moessner, R. & Chalker, J. T. Properties of a Classical Spin Liquid: The Heisenberg Pyrochlore Antiferromagnet. *Physical Review Letters* **80**, 2929–2932 (1998).
5. Canals, B. & Lacroix, C. Pyrochlore Antiferromagnet: A Three-Dimensional Quantum Spin Liquid. *Physical Review Letters* **80**, 2933–2936 (1998).
6. Tsunetsugu, H. Antiferromagnetic Quantum Spins on the Pyrochlore Lattice. *Journal of the Physical Society of Japan* **70**, 640–643 (2001).
7. Bramwell, S. T., Gingras, M. J. P. & Reimers, J. N. Order by disorder in an anisotropic pyrochlore lattice antiferromagnet. *J Appl Phys* **75**, 5523–5525 (1994).
8. Bergman, D. L., Shindou, R., Fiete, G. A. & Balents, L. Models of degeneracy breaking in pyrochlore antiferromagnets. *Physical Review B* **74**, 9 (2006).
9. Bellier-Castella, L., Gingras, M. J., Holdsworth, P. C. & Moessner, R. Frustrated order by disorder: The pyrochlore anti-ferromagnet with bond disorder. *Can J Phys* **79**, 1365–1371 (2001).
10. Tchernyshyov, O., Moessner, R. & Sondhi, S. L. Order by Distortion and String Modes in Pyrochlore Antiferromagnets. *Physical Review Letters* **88**, 067203 (2002).
11. Bramwell, S. T. Spin Ice State in Frustrated Magnetic Pyrochlore Materials. *Science* **294**, 1495–1501 (2001).
12. Lee, S. H. *et al.* Emergent excitations in a geometrically frustrated magnet. *Nature* **418**, 856–858 (2002).
13. Bai, X. *et al.* Magnetic Excitations of the Classical Spin Liquid MgCr_2O_4 . *Phys Rev Lett* **122**, 097201 (2019).
14. Hallas, A. M., Gaudet, J. & Gaulin, B. D. Experimental Insights into Ground-State Selection of Quantum XY Pyrochlores. *Annu Rev Condens Matter Phys* **9**, 105–124 (2018).
15. Rau, J. G. & Gingras, M. J. P. Frustrated Quantum Rare-Earth Pyrochlores. *Annu Rev Condens Matter Phys* **10**, 357–386 (2019).

16. Kimura, K., Nakatsuji, S. & Kimura, T. Experimental realization of a quantum breathing pyrochlore antiferromagnet. *Physical Review B* **90**, 060414 (2014).
17. Okamoto, Y., Nilsen, G. J., Attfield, J. P. & Hiroi, Z. Breathing Pyrochlore Lattice Realized in A-Site Ordered Spinel Oxides $\text{LiGaCr}_4\text{O}_8$ and $\text{LiInCr}_4\text{O}_8$. *Physical Review Letters* **110**, 097203 (2013).
18. Li, F.-Y. *et al.* Weyl magnons in breathing pyrochlore antiferromagnets. *Nature Communications* **7**, 12691 (2016).
19. Yan, H., 闫寒, Benton, O., Jaubert, L. D. C. & Shannon, N. Rank-2 U(1) Spin Liquid on the Breathing Pyrochlore Lattice. *Phys Rev Lett* **124**, 127203 (2020).
20. Lee, S. *et al.* Multistage symmetry breaking in the breathing pyrochlore lattice $\text{Li}(\text{Ga,In})\text{Cr}_4\text{O}_8$. *Physical Review B* **93**, 174402 (2016).
21. Okamoto, Y., Nilsen, G. J., Nakazono, T. & Hiroi, Z. Magnetic Phase Diagram of the Breathing Pyrochlore Antiferromagnet $\text{LiGa}_{1-x}\text{In}_x\text{Cr}_4\text{O}_8$. *Journal of the Physical Society of Japan* **84**, 043707 (2015).
22. Wawrzyńczak, R. *et al.* Classical Spin Nematic Transition in $\text{LiGa}_{0.95}\text{In}_{0.05}\text{Cr}_4\text{O}_8$. *Physical Review Letters* **119**, 087201 (2017).
23. Okamoto, Y. *et al.* Magnetic transitions under ultrahigh magnetic fields of up to 130 T in the breathing pyrochlore antiferromagnet $\text{LiInCr}_4\text{O}_8$. *Physical Review B* **95**, 134438 (2017).
24. Ran, Y., Hermele, M., Lee, P. A. & Wen, X.-G. Projected-Wave-Function Study of the Spin-1/2 Heisenberg Model on the Kagomé Lattice. *Physical Review Letters* **98**, 117205 (2007).
25. Ryu, S., Motrunich, O. I., Alicea, J. & Fisher, M. P. A. Algebraic vortex liquid theory of a quantum antiferromagnet on the kagome lattice. *Phys Rev B* **75**, 184406 (2007).
26. Fichtl, R. *et al.* Orbital Freezing and Orbital Glass State in FeCr_2S_4 . *Phys Rev Lett* **94**, 027601 (2005).
27. Silverstein, H. J. *et al.* Liquidlike correlations in single-crystalline $\text{Y}_2\text{Mo}_2\text{O}_7$: An unconventional spin glass. *Physical Review B* **89**, 054433 (2014).
28. Tanaka, Y., Yoshida, M., Takigawa, M., Okamoto, Y. & Hiroi, Z. Novel Phase Transitions in the Breathing Pyrochlore Lattice: ^7Li -NMR on $\text{LiInCr}_4\text{O}_8$ and $\text{LiGaCr}_4\text{O}_8$. *Physical Review Letters* **113**, 227204 (2014).
29. Baek, S. H., Choi, K. Y., Berger, H., Büchner, B. & Grafe, H. J. Persistence of singlet fluctuations in the coupled spin tetrahedra system $\text{Cu}_2\text{Te}_2\text{O}_5\text{Br}_2$ revealed by high-field magnetization, ^{79}Br NQR, and ^{125}Te NMR. *Physical Review B* **86**, 180405 (2012).

30. Shimizu, T., MacLaughlin, D. E., Hammel, P. C., Thompson, J. D. & Cheong, S.-W. Spin susceptibility and low-lying excitations in the Haldane-gap compound Y_2BaNiO_5 . *Phys Rev B* **52**, R9835–R9838 (1995).
31. Furukawa, Y., Iwai, A., Kumagai, K. & Yakubovsky, A. ^{31}P -NMR Study of Low-Energy Spin Excitations in Spin Ladder $(\text{VO})_2\text{P}_2\text{O}_7$ and Spin Dimer $\text{VO}(\text{HPO}_4)_{0.5}\text{H}_2\text{O}$ Systems. *J Phys Soc Jpn* **65**, 2393–2396 (1996).
32. Uemura, Y. J., Yamazaki, T., Harshman, D. R., Senba, M. & Ansaldo, E. J. Muon-spin relaxation in AuFe and CuMn spin glasses. *Physical Review B* **31**, 546–563 (1985).
33. Li, Y. *et al.* Muon Spin Relaxation Evidence for the U(1) Quantum Spin-Liquid Ground State in the Triangular Antiferromagnet YbMgGaO_4 . *Physical Review Letters* **117**, 097201 (2016).
34. Balz, C. *et al.* Physical realization of a quantum spin liquid based on a complex frustration mechanism. *Nature Physics* **12**, 942–949 (2016).
35. Mendels, P. *et al.* Quantum Magnetism in the Paratacamite Family: Towards an Ideal Kagomé Lattice. *Physical Review Letters* **98**, 077204 (2007).
36. Yaouanc, A. & Réotier, P. D. de. *Muon Spin Rotation, Relaxation, and Resonance: Applications to Condensed Matter*. vol. 147 (Oxford University Press, 2013).
37. Hemmida, M., Nidda, H. A. K. von, Tsurkan, V. & Loidl, A. Berezinskii-Kosterlitz-Thouless type scenario in the molecular spin liquid ACr_2O_4 ($A = \text{Mg}, \text{Zn}, \text{Cd}$). *Physical Review B* **95**, 1144 (2017).
38. Kimchi, I., Nahum, A. & Senthil, T. Valence Bonds in Random Quantum Magnets: Theory and Application to YbMgGaO_4 . *Physical Review X* **8**, 1 (2018).
39. Nilsen, G. J. *et al.* Complex magnetostructural order in the frustrated spinel $\text{LiInCr}_4\text{O}_8$. *Physical Review B* **91**, 174435 (2015).
40. Tol, J. van, Brunel, L. C. & Wylde, R. J. A quasioptical transient electron spin resonance spectrometer operating at 120 and 240 GHz. *Review of Scientific Instruments* **76**, 074101 (2005).

Figures

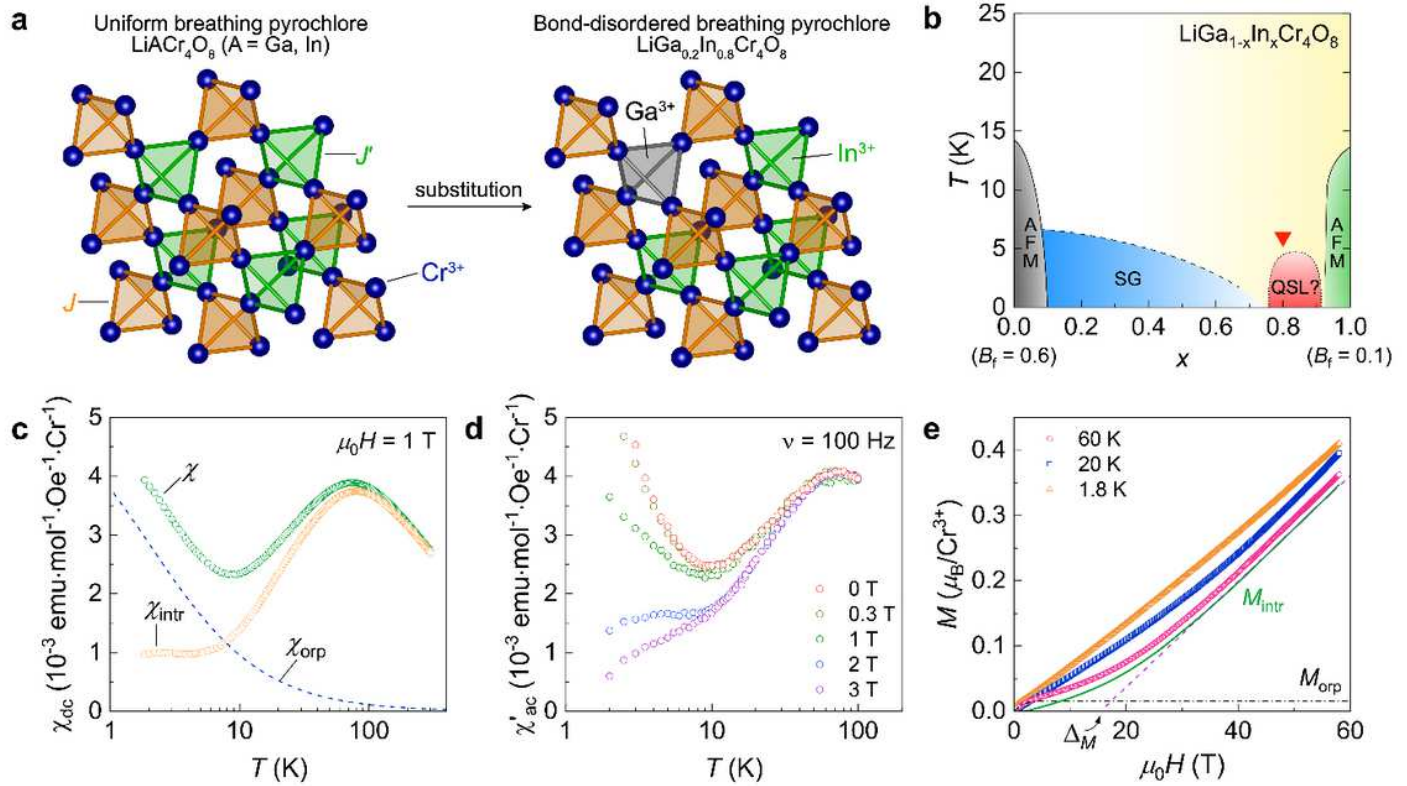


Figure 1

Crystal structure, phase diagram, and magnetic properties. a Schematic structure of the uniform breathing pyrochlore LiACr_4O_8 ($A = \text{Ga, In}$) and the bond-disordered breathing pyrochlore $\text{LiGa}_{0.2}\text{In}_{0.8}\text{Cr}_4\text{O}_8$. b T-x phase diagram of $\text{LiGa}_{1-x}\text{In}_x\text{Cr}_4\text{O}_8$. The inverse red triangle marks the investigated compound $\text{LiGa}_{0.2}\text{In}_{0.8}\text{Cr}_4\text{O}_8$. c Temperature dependence of the static magnetic susceptibility $\chi_{dc}(T)$ of $\text{LiGa}_{0.2}\text{In}_{0.8}\text{Cr}_4\text{O}_8$. $\chi_{dc}(T)$ is decomposed into the intrinsic $\chi_{intr}(T)$ and the orphan spin contribution $\chi_{orp}(T)$. d Real component of the ac magnetic susceptibility $\chi'_{ac}(T)$ as a function of T and B measured with a fixed frequency of $\nu = 100 \text{ Hz}$. e High-field magnetization measured at selected temperatures. The black dashed-dotted and green dashed lines indicate the orphan spin magnetization $M_{orp}(T)$ and the bulk magnetization $M_{intr}(T)$. A linear extrapolation gives the spin gap of $\Delta_M/k_B \sim 20 \text{ K}$.

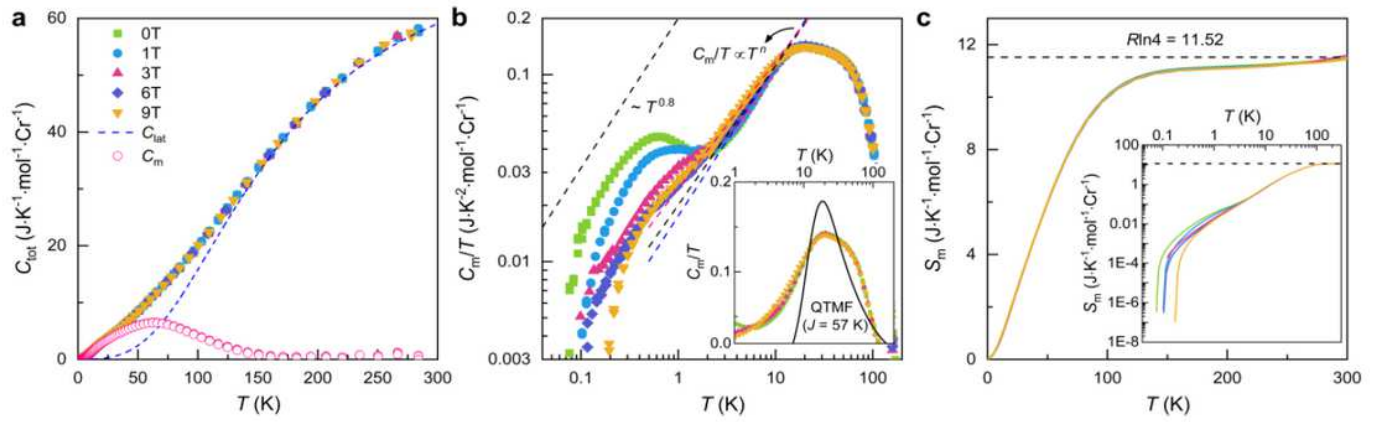


Figure 2

Heat capacity of the breathing pyrochlore $\text{LiGa}_{0.2}\text{In}_{0.8}\text{Cr}_4\text{O}_8$. a Temperature dependence of the total heat capacity C_{tot} in various magnetic fields $B=0, 1, 3, 6,$ and 9 T. The blue dashed curve denotes the evaluated lattice contributions using the Debye model. The open pink circles represent the magnetic heat capacity C_m . b Temperature and field dependences of the magnetic heat capacity divided by temperature C_m/T after subtracting the lattice and nuclear Schottky contributions on a double log scale. The dashed lines are fits to the power-law behavior $C_m/T \sim T^n$ with $n = 0.68 - 0.82$. The inset shows a comparison between the C_m/T data and the theoretical curve for a $s=3/2$ tetrahedron model. c Temperature dependence of the magnetic entropy S_m under various magnetic fields. The dashed black line corresponds to the theoretical value $R\ln 4 = 11.52$. The inset is a log-log plot of S_m vs. temperature.

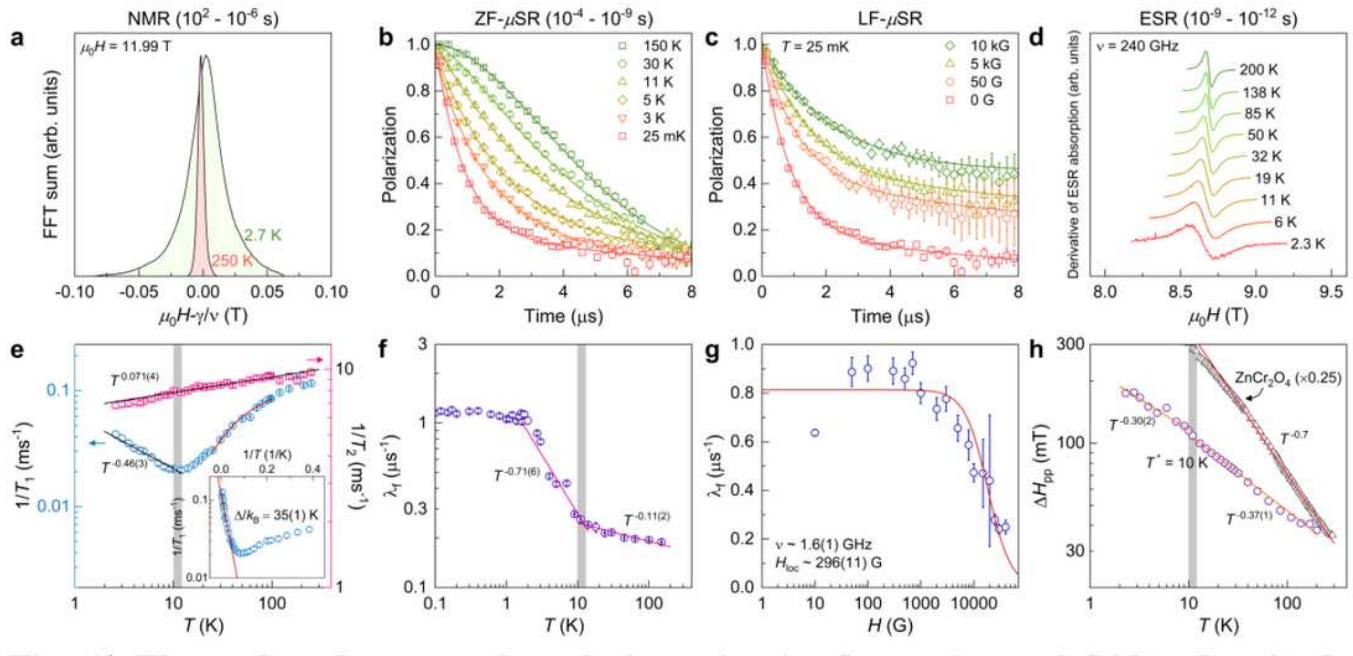


Figure 3

Thermal and temporal evolution of spin fluctuations of $\text{LiGa}_{0.2}\text{In}_{0.8}\text{Cr}_4\text{O}_8$ measured by ^7Li NMR, ZF- μSR , and ESR. a ^7Li NMR spectra obtained by integrating spin-echo intensity at $T = 2.7$ and 250 K. b ZF-

μ SR spectra at selected temperatures. c Longitudinal field dependence of the μ SR spectra measured at $T = 25$ mK. The solid lines denote the fit to the data using the sum of two simple exponential functions. d Derivative of the ESR absorption spectra measured at various temperatures. Spectra are vertically shifted for clarity. e Temperature dependence of ${}^7\text{Li}$ spin-lattice relaxation rate $1/T_1$ and spin-spin relaxation rate $1/T_2$. The red solid line denotes the Arrhenius equation, yielding the spin gap of $\Delta/k_B = 35(1)$ K. The solid black line represents a power-law behavior of $1/T_1$ and $1/T_2$. f Muon spin relaxation rate as a function of temperature $\lambda f(T)$. The solid magenta line represents the power-law fit to the data. g Muon spin relaxation as a function of longitudinal field $\lambda LF(H)$. The red solid line represents the fit to the Redfield formula. h Temperature dependence of the peak-to-peak ESR linewidth $\Delta H_{pp}(T)$. The solid orange lines indicate a power-law behavior of $\Delta H_{pp}(T)$ in two different temperature regions. The shaded region indicates the change of magnetic correlations at around $T^* = 10$ K.

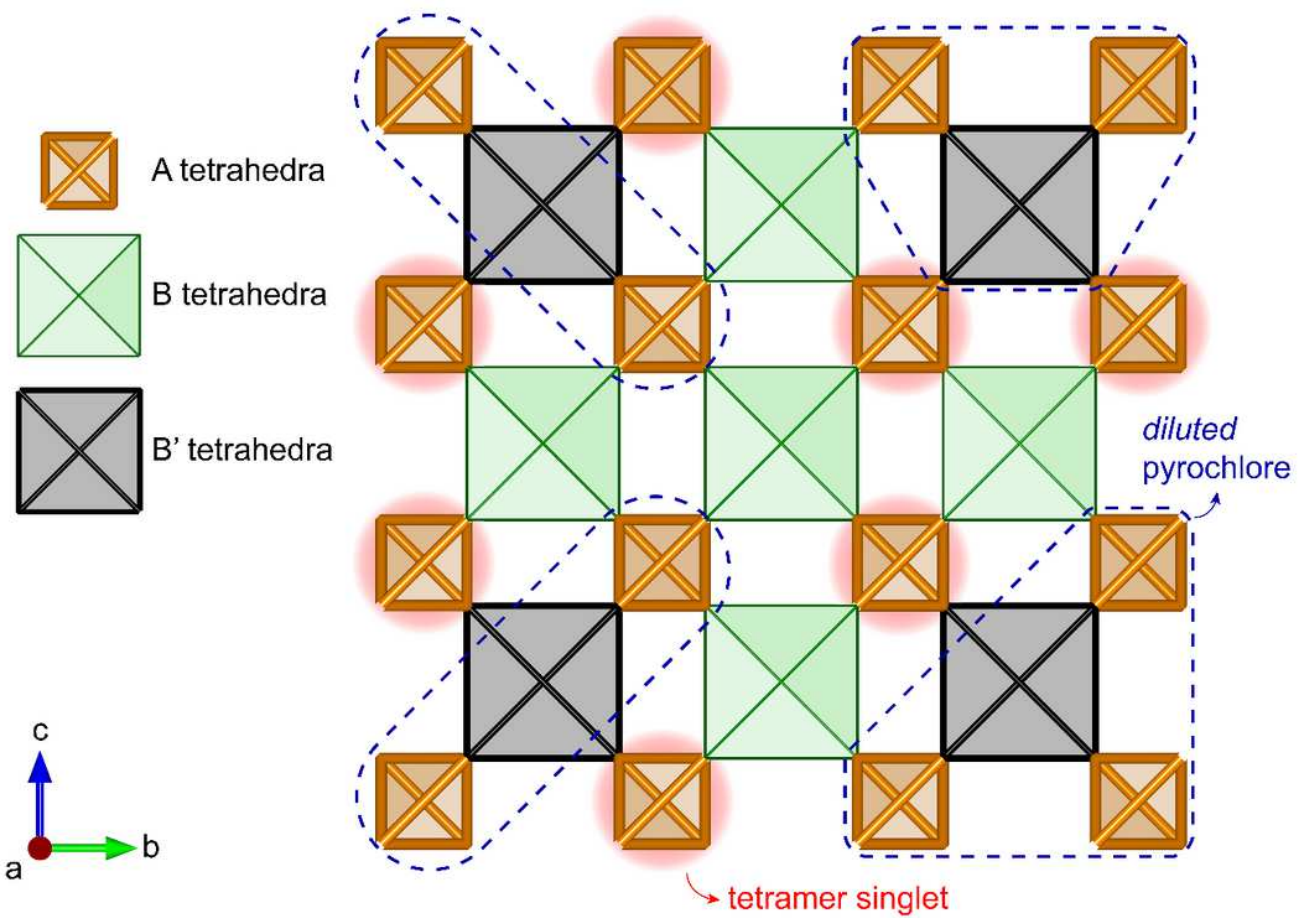


Figure 4

Schematics of the emergent magnetic subsystems in a bond-disordered breathing pyrochlore. Each square represents the tetrahedra formed by the Cr spins. The Cr spins are omitted for clarity. The orange and green squares are the alternating A and B tetrahedra for $\text{LiInCr}_4\text{O}_8$. The grey square denotes the B' tetrahedra introduced by the Ga-for-In substitution. Due to an energy hierarchy of the tetrahedral ($E_A \sim E_{B'} > E_B$), the breathing pyrochlore is effectively decomposed into two subsystems: (i) coupled tetramer singlets (red shaded circle) and (ii) diluted pyrochlore lattices (blue dashed region).

Supplementary Files

This is a list of supplementary files associated with this preprint. Click to download.

- [Supplementaryinformation.pdf](#)